CLADISS—A Longitudinal Multimode Model for the Analysis of the Static, Dynamic, and Stochastic Behavior of Diode Lasers with Distributed Feedback

PATRICK VANKWIKELBERGE, GEERT MORTHIER, AND ROEL BAETS, MEMBER, IEEE

Abstract—A new computer model called CLADISS is presented for the analysis of multisection diode lasers. The model allows for the analysis of a wide variety of multisection devices with discrete or distributed internal reflections. The simulator can carry out a threshold, dc, ac, and a noise analysis. The threshold analysis determines the threshold of the various longitudinal modes of the laser. The power versus current and the wavelength versus current characteristics are found with the self-consistent dc analysis. In each of the dc bias points the dynamic ac analysis can calculate the FM and AM response of the laser, while the noise analysis can determine the frequency and intensity noise spectra, and the line shape of the longitudinal modes. Not only do the dc, ac, and noise analyses consider several longitudinal modes simultaneously, but they also take into account nonlinear gain suppression, spontaneous emission, and longitudinal spatial hole burning. CLADISS includes all of the longitudinal variations by dividing each laser section in many short segments. Both the optical field and carrier density are discretized according to this segmentation.

To demonstrate the capabilities of CLADISS some nonlinear effects in DFB lasers are treated. We first consider instabilities induced in the side-mode suppression ratio by spatial hole burning. Next we discuss the effects of spatial hole burning and side modes on the FM response and on the linewidth. Finally, the model is used to calculate the linewidth floor due to the power dependence of the linewidth enhancement factor.

I. INTRODUCTION

CONSIDERABLE research is currently being performed in the field of optical coherent communication systems. Such optical systems require dynamic single-mode diode lasers with a narrow linewidth as well as wide tuning range when used as a local oscillator. In view of meeting those demands new devices, such as C^3, DFB, DBR, extended cavity lasers, and so on, were developed. However, the complete behavior of these devices is not always fully understood. Furthermore, one is interested in knowing for which combination of geometrical structure and material composition a specific type of laser cavity behaves optimally. Simple analytic formulations can-

not give a satisfactory answer to many of these questions. More and more research groups are therefore putting an increased effort in computer-assisted laser diode modeling [1]–[6], not only to explain the behavior of existing devices but also to predict the behavior of future devices still on the "design table."

We developed a new diode laser simulator, called CLADISS, which stands for "compound cavity laser diode simulation software." With CLADISS all previous mentioned types of devices can be analyzed and the simulator is sufficiently general to investigate a variety of other, multisection diode lasers. CLADISS can carry out a threshold analysis, a static above-threshold dc analysis, a dynamic small-signal ac analysis, and a linewidth calculation. Characteristic to all of these types of analyses is that they consider several longitudinal modes simultaneously. Moreover, in the dc, ac, and noise analyses, nonlinear gain suppression, longitudinal spatial hole burning, and spontaneous emission are taken into account accurately. CLADISS includes all longitudinal variations, in particular spatial hole burning, by dividing each laser section into many short segments. Both the optical field and carrier density are discretized according to this segmentation. By means of the CLADISS analysis tool, we are able to calculate the laser threshold, the output power and wavelength versus current characteristics of the different modes, the FM and the AM response in any dc bias point, as well as the frequency and intensity noise spectra, and the linewidth and line shape of each mode of a dc solution.

In this paper we present the CLADISS package. We first describe how the laser is decomposed in several sections. Next the mathematical description of a section is given by means of a carrier rate equation and a set of coupled traveling-wave rate equations, which incorporate spontaneous emission and noise. In the following sections each of the four types of analysis is presented in more detail. Finally, to demonstrate the capabilities of CLADISS, we discuss some important issues related to DFB lasers: instabilities in the side-mode rejection induced by spatial hole burning [1], [5], the spatial hole burning contribution to the FM response [7], and the linewidth satu-

ration at high-power levels. We also confirm our earlier statement that for DFB lasers with a good mode rejection ratio (greater than 30 dB at a 5 mW output power) the linewidth floor is mainly due to nonlinear gain saturation [8], [9].

II. THE LASER STRUCTURE

Most existing diode lasers can be decomposed into a cascade of sections which have uniform structural dimensions and material properties along the longitudinal direction. Gratings form one exception to this but they are generally considered as a small perturbation of a longitudinally uniform structure. In our model a laser structure is therefore described as a concatenation of longitudinally uniform sections, each of which can have different material or geometrical properties. At the transition between two sections there can be discrete reflections and these are represented by what we call interface elements. Therefore each laser forms a cascade of sections and interface elements. Fig. 1 shows a laser with four sections. We also drew the corresponding cascade. Notice that interface elements are only used if a misadaption effectively occurs. The boundaries of the laser cavity are also considered to be interface elements connecting the laser cavity to the outside.

In the current implementation all the laser sections in CLADISS are "current controlled," i.e., the electrical excitation, if any, of a section is induced by a current source.

III. THE MATHEMATICAL DESCRIPTION OF THE LASER

We assume that each section waveguide only sustains the lowest TE mode. In each section the forward (+) and backward (−) propagating parts of the lateral electrical laser field, consisting of several longitudinal modes, are represented by

$$E_y^{\pm}(x, y, z, t)$$

$$= \Phi(x, y) \, \text{Re} \left[\sum_q E_q^{\pm}(z, t) \exp \left(j\omega_q t \mp j\beta_{rq}z \right) \right].$$

$$(1)$$

For all of the longitudinal modes q the same transverse-lateral field distribution $\Phi(x, y)$ is used. The function Φ is assumed to be independent of time and the axial position in the section. The frequency ω_q is the reference frequency of the phasor notation used for the quasi-time harmonic fields of the qth longitudinal mode and must be chosen close enough to the frequency region where lasing is expected to occur. The amplitudes $E_q^{\pm}$ will then vary slowly in time with respect to ω_q and it is the time variation of the phase of $E_q^{\pm}$ that determines the lasing frequencies of the spectral field components. Similarly β_{rq} is a reference propagation constant. In case the section contains no grating β_{rq} is set equal to the propagation constant β_q at the reference frequency ω_q of the lowest TE mode of the unperturbed waveguide, i.e., the waveguide with-
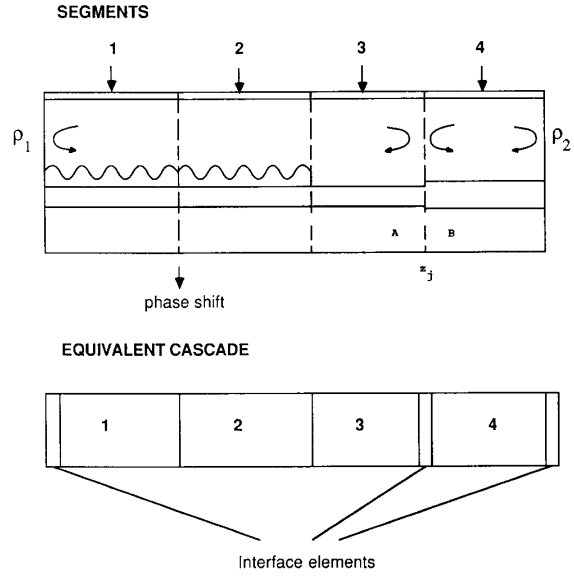
Fig. 1. General structure of a multisection laser and its equivalent cascade.

out loss or gain. When a grating is present β_{rq} is set equal to the Bragg wavenumber $\beta_g = m\pi/\Lambda$, in which m is the order of the grating. In that way the fast spatial variation is removed from the complex amplitudes $E_q^{\pm}$ in both cases.

For each position along the cavity, a set of forward and backward instantaneous frequencies $\tilde{\omega}_q^{\pm}(z, t)$ can be defined:

$$\tilde{\omega}_q^{\pm}(z, t) = \omega_q + \frac{\partial}{\partial t} \arg \left[E_q^{\pm}(z, t) \right]. \qquad (2)$$

However, if the dynamic excitation is slow as compared to the round-trip time of the laser, then the instantaneous frequencies will hardly vary along the cavity. Therefore the instantaneous frequencies $\tilde{\omega}_q^+$ or $\tilde{\omega}_q^-$ at any position along the laser can be used to represent the lasing frequency $\tilde{\omega}_q(t)$ of the qth mode. We will take the instantaneous frequency of the backward field at the left-hand facet. The origin of the z axis is chosen at this facet, so that $\tilde{\omega}_q$ becomes

$$\tilde{\omega}_q(t) = \tilde{\omega}_q^-(z = 0, t) = \omega_q + \Delta\omega_q(t). \qquad (3)$$

The second equality defines the difference $\Delta\omega_q = \tilde{\omega}_q - \omega_q$, used further on. In all the complex refractive index perturbations due to the carrier injection, we will apply this frequency $\tilde{\omega}_q(t)$.

The complex amplitudes $E_q^{\pm}(z, t)$ are transformed into new complex amplitudes $R_q^{\pm}(z, t)$ by the relationship

$$E_q^{\pm}(z, t) = R_q^{\pm}(z, t) \exp \left[\int^t \Delta\omega_q(\tau) \, d\tau \right]$$

with

$$R_q^{\pm}(z, t) = r_q^{\pm}(z, t) \exp \left[j\phi_q^{\pm}(z, t) \right]$$

$$\phi_q^-(z = 0, t) = 0. \qquad (4)$$

Both $r_q^{\pm}$ and $\phi_q^{\pm}$ are real functions of z and t. The chirp or FM of a mode is now no longer included in the field amplitudes $R_q^{\pm}$, but appears explicitly in the extra variable $\Delta\omega_q$. This extra variable induces an extra equation which fixes the phase $\phi_q^-(z = 0, t)$ to a constant value, i.e., zero.

For each mode, with modal amplitudes $R_q^{\pm}(z, t)$, a set of coupled traveling-wave rate equations can now be derived from Maxwell's equations using the slowly-varying amplitude approximations [10] and the approximations related to the coupled-mode theory [11]. We then obtain

$$\frac{\partial R_q^+}{\partial z} + \frac{1}{v_{gq}}\frac{\partial R_q^+}{\partial t} + \left(j\frac{\Delta\omega_q}{v_{gq}} + j\Delta\beta_q - \frac{J_{sp}}{|R_q^+|^2} \right) R_q^+$$

$$= j\kappa^+ R_q^- + F_q^+$$

$$-\frac{\partial R_q^-}{\partial z} + \frac{1}{v_{gq}}\frac{\partial R_q^-}{\partial t} + \left(j\frac{\Delta\omega_q}{v_{gq}} + j\Delta\beta_q - \frac{J_{sp}}{|R_q^-|^2} \right) R_q^-$$

$$= j\kappa^- R_q^+ + F_q^- \tag{5}$$

with

$$\Delta\beta_q = \beta_q - \beta_{rq} + \Gamma\Delta\gamma - 0.5j\alpha_{int}$$

$$\Delta\gamma = \frac{\omega_q^2}{c^2\beta_q} n_a \left(\Delta n_r + j\frac{g}{2k_q} \right)$$

$$g = A(\tilde{\omega}_q)\left(N - N_{tq}(\tilde{\omega}_q)\right)\left(1 - \sum \epsilon_{sp}(\tilde{\omega}_q, \tilde{\omega}_p)P_p\right)$$

$$\Delta n_r = 2k_q[-\alpha_{lw,0}(\tilde{\omega}_q) A(\tilde{\omega}_q) N(z, t) + B(\tilde{\omega}_q)]$$

$$\alpha_{int} = \alpha_0(\tilde{\omega}_q) + \alpha_1(\tilde{\omega}_q) N(z, t)$$

$$P_p(z, t) = |R_p^+|^2 + |R_p^-|^2. \tag{6}$$

In these expressions one can distinguish two types of parameters. First, there are those parameters ($\kappa^{\pm}$, v_{gq}, $\cdots$,) which are slow functions of frequency. They are explained in Table I and are assumed to be constant with a value taken at the reference frequencies ω_q. If no grating occurs the $\kappa^{\pm}$ coupling coefficients are set to zero. The phase of $\kappa^{\pm}$ depends on the relative position of the grating with respect to the origin of the z axis. Furthermore, for pure index gratings $\kappa^+ = (\kappa^-)^*$ and for pure-gain gratings $\kappa^+ = -(\kappa^-)^*$. For a combination of both index and gain gratings the $\kappa^{\pm}$ can be split into two parts corresponding, respectively, to index and gain grating effects [12], [13]. The following assumptions are implied by the slowly-varying amplitude approximation:

$$\Delta\omega_q \ll \omega_q \qquad \Delta\beta_q \ll \beta_{rq}. \tag{7}$$

Both conditions are fulfilled if ω_q and β_{rq} are chosen as mentioned above.

Second, there are a number of parameters which vary rapidly with frequency. For these parameters the frequency dependence is taken into account. The function g expresses the power gain in the active region at the in-

TABLE I

Parameter		Typical Value	
w	(μm)	1.5	Stripe Width
d	(μm)	0.12	Active Layer Thickness
Γ		0.5	Power Confinement Factor in Active Layer
κ^+	(μm^{-1})		Coupling Coefficient—Backward to Forward Propagating Wave
κ^-	(μm^{-1})		Coupling Coefficient—Forward to Backward Propagating Wave
L	(μm)	± 300	Laser Length
λ_q	(μm)		Wavelength of the qth Mode
Λ	(μm)	0.2413	Grating Period
n_e		3.25	Unperturbated Effective Refractive Index
α_{int}	(μm^{-1})	$50 \cdot 10^{-4}$	International Waveguide Losses
v_{gq}	(μm/s)	$7.46 \cdot 10^{13}$	Group Velocity
ρ_b			Field Reflectivity at Left (or Back) Facet
ρ_f			Field Reflectivity at Right (or Front) Facet
ϕ_{mf}		$(-\pi, \pi)$	Phase of Reflectivity ρ_f
ϕ_{mb}		$(-\pi, \pi)$	Phase of Reflectivity ρ_b
R_b		0.32	Power Reflectivity at Left Facet
R_f		0, 0.05, 0.32	Power Reflectivity at Right Facet
β_{xp}		10^{-4}	Spontaneous Emission Factor
n_{sp}		2	Inversion Factor
η		0.8	Current Injection Efficiency
q	(Coulomb)	$1.6 \cdot 10^{-19}$	Electron Charge
τ	(s)	$5 \cdot 10^{-9}$	Carrier Lifetime
B	(μm^3/s)	100	Biomolecular Recombination
C	(μm^6/s)	$20 \cdot 10^{-5}$	Auger Recombination

stantaneous frequency $\tilde{\omega}_q(t)$ of the qth laser mode. Nonlinear gain suppression at $\tilde{\omega}_q$ resulting from all the modes is included via the $(1 - \sum \epsilon_{sp}P_p)$ factor. P_p is expressed in watts, which implies that the $|R_p^{\pm}|^2$ are power normalized; ϵ_{sp} can for instance be attributed to spectral hole burning or to the gratings induced by the cavity standing waves. The function Δn_r expresses the change in the real part of the refractive index associated with the carrier injection and can be linked to the linear gain via $\alpha_{lw,0}$. The α_{int} term represents the internal losses. In 1.55 μm lasers they mainly consist of intervalence band absorption [14]. The functional dependencies of g, Δn_r, and α_{int} on $\tilde{\omega}_q$ and the carrier density $N(z, t)$ are given by analytic functions found through curve fittings on the numerical results obtained with the material models of [14] and [15].

The $J_{sp}/|R_q^{\pm}|^2$ terms represent the local average spontaneous emission that couples into the forward, respectively, backward propagating waves of the qth mode. The spontaneous emission is written here as a contribution to the gain and is a nonlinear term. The justification for describing the spontaneous emission in that manner is given in Appendix I. Its inclusion is necessary to model mode competition accurately in a multimode above-threshold analysis. For power-normalized field intensities the J_{sp} coefficient is written as

$$J_{sp} = \tfrac{1}{4}wd\beta_{sp}(\hbar\omega_q) BN^2(z, t). \tag{8}$$

Again we refer to Table I for an explanation of the parameters. Note that BN^2 represents the radiative spontaneous

recombination and that β_{sp} is the spontaneous emission factor [16].

The $F_q^\pm(z, t)$ terms are the Langevin force functions which represent the photon shot noise. The statistical processes related to these force functions can be approximated by Gaussian processes [17], [18]. In that case the Langevin functions are completely determined by their first- and second-order moments, which will be given in Section V-D, when discussing the noise analysis in detail.

When two adjacent sections have misadapted waveguides an interface element is introduced to describe the boundary condition between the two guides. For two waveguides A and B joining each other at the axial position z_j of the jth interface (see Fig. 1) the boundary conditions become

$$\begin{pmatrix} R_q^+ \\ R_q^- \end{pmatrix}(z_j, t)_B = \frac{1}{t_j}\begin{pmatrix} 1 & -\rho_j \\ -\rho_j & 1 \end{pmatrix}\begin{pmatrix} R_q^+ \\ R_q^- \end{pmatrix}(z_j, t)_A. \quad (9)$$

For the boundary conditions at the ends ($z = 0$ and $z = L$) of the laser cavity we use

$$R_q^+(0, t) = \rho_b R_q^-(0, t)$$

$$R_q^-(L, t) = \rho_f R_q^+(L, t). \quad (10)$$

Remember that at $z = 0$ the additional relation $\phi_q^-(z = 0, t) = 0$ holds.

The g, Δn_r, α_{int}, and J_{sp} quantities in the above wave equations all depend on the carrier density $N(z, t)$ in the active region. Due to spatial hole burning $N(z, t)$ can vary with position within a section. The carrier dynamics are given by the following rate equation:

$$\frac{\partial N}{\partial t} = \frac{\eta J}{qd} - \frac{N}{\tau} - BN^2 - CN^3 - \sum_q \frac{\Gamma g(N, \tilde{\omega}_q)}{(\hbar\omega_q)wd}$$

$$\cdot \left(|R_q^+|^2 + |R_q^-|^2 \right) + F_N(z, t). \quad (11)$$

Table I explains all of the parameters; J is the injected current density and is taken uniform throughout the whole section. The longitudinal diffusion term has been neglected in (11) because the diffusion length is usually short as compared to the longitudinal variations of N. The function $F_N(z, t)$ is the Langevin force function representing the carrier shot noise, which is also assumed Gaussian. Its relevant moments are given in Section V-D. Fluctuations of the injected current and $1/f$ noise can also be taken into account.

Equations (1)–(11) determine the static, dynamic, and stochastic behavior of a large class of multisection diode lasers. The main limitations are that only current controled sections are used, that strong lateral and transverse confinement of the carriers and the fields is assumed and that only the lowest TE mode is considered.

Finally we ought to mention that no thermal effects are included in the implementation presented here.

IV. STRUCTURED ANALYSIS OF A DIODE LASER

Table II shows the four types of analysis versus four characteristic elements of the mathematical description.

TABLE II

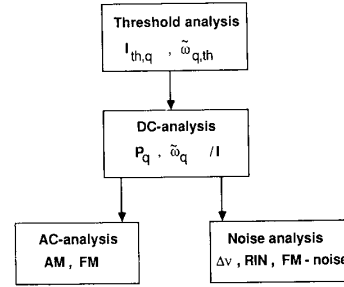| Analysis	Spontaneous Emission J_{sp}	Stimulated Recombination	Dynamics (t-Derivative)	Nonlinear Gain Suppression
Threshold	−	−	−	−
dc	+	+	−	+
ac	+	+	+	+
Stochastic	+	+	+	+

Fig. 2. Simulation procedure to be followed when using CLADISS.

The crosses (+) in Table II indicate which of the four characteristics are taken into account by each analysis.

The first step in the investigation of a diode laser with CLADISS should be a threshold analysis, that determines the threshold currents and wavelengths of several longitudinal modes. The threshold analysis also indicates which modes, besides the main mode, we should consider in the dc analysis, by calculating the threshold gain differences between the main mode and the side modes.

Next, a dc analysis can be executed. This is a self-consistent static analysis that calculates the power versus current and the wavelength versus current characteristics of the laser. Each point of these characteristics is calculated iteratively and uses the former point as an initial estimate. Therefore, successive points must be close to each other to obtain good convergence and the first point should be taken close to threshold because we can then use the threshold solution to find a good initial estimate for this starting point.

Both the ac and stochastic analysis use a small-signal approximation. This approximation allows the linearization of all of the dynamic equations around some bias point, which can be any point of the dc solution. Therefore, prior to the ac or noise analysis the dc calculation must be executed.

Fig. 2 summarizes the procedure to be followed when studying a diode laser with CLADISS. It also gives an overview of the various characteristics calculated by each analysis. In the next sections we discuss each of the four types of analysis.

V. NUMERICAL IMPLEMENTATION

A. The Threshold Analysis

Consider a laser with m_s sections and take the current I_v of the vth section as the independent variable current

source. The currents in the $(m_s - 1)$ other sections are assumed to be of the form

$$I_j = a_j I_v + i_j > 0 \qquad a_j \geqq 0 \qquad (12)$$

in which a_j and i_j are user-specified parameters. The threshold analysis searches for the threshold values of I_v, i.e., those values of I_v for which there exists at least one frequency $\tilde{\omega}_q$ such that the amplitude and phase resonance conditions of the cavity are fulfilled.

The amplitude and phase resonances are defined as follows. Take some point z_v somewhere along the cavity. As Fig. 3 shows, the cavity is then divided into two parts, which can be replaced by effective reflectivities, respectively, ρ_L for the left-hand part and ρ_R for the right-hand part. Those reflectivities depend on the frequency $\tilde{\omega}_q$ and the current I_v. Using the complex round-trip gain $\rho_L \rho_R$, the phase and amplitude resonance conditions are expressed by

$$\rho_L(\tilde{\omega}_q, I_v) \, \rho_R(\tilde{\omega}_q, I_v) - 1 = 0. \qquad (13)$$

In this way the threshold analysis reduces to the search of the roots $(\tilde{\omega}_{q,\text{th}}, I_{\text{th},q})$ of (13). The couple with the lowest threshold current $I_{\text{th},q}$ defines the laser threshold.

The reflection coefficients ρ_L and ρ_R are calculated by means of the propagator matrices $\bar{\bar{F}}_L(\tilde{\omega}_q, I_v)$ and $\bar{\bar{F}}_R(\tilde{\omega}_q, I_v)$ [2], [19] of the left-hand and right-hand parts of the cavity (Fig. 3):

$$\rho_L = \frac{\rho_1(\bar{\bar{F}}_L)_{11} + (\bar{\bar{F}}_L)_{12}}{\rho_1(\bar{\bar{F}}_L)_{21} + (\bar{\bar{F}}_L)_{22}}$$

$$\rho_R = -\frac{\rho_2(\bar{\bar{F}}_R)_{12} - (\bar{\bar{F}}_R)_{22}}{\rho_2(\bar{\bar{F}}_R)_{11} - (\bar{\bar{F}}_R)_{21}}. \qquad (14)$$

Because the stimulated recombination is omitted in the threshold analysis (i.e., no gain suppression or spatial hole burning occur), the propagator matrices can be calculated straightforwardly without any iteration techniques, once a frequency $\tilde{\omega}_q$ and a set of section currents are specified.

CLADISS solves (13) by means of a two-step procedure. First, good initial estimates of the most important roots, i.e., the lasing mode and its nearest sidemodes, are traced by a scanning procedure, that is applied to a sufficiently-wide frequency window in the $(\tilde{\omega}_q, I_v)$-plane. Second, with the obtained estimates a Newton–Raphson iteration is initiated. The derivatives $\partial \rho_L/\partial \tilde{\omega}_q$, $\partial \rho_R/\partial \tilde{\omega}_q$, $\partial \rho_L/\partial I_v$, and $\partial \rho_R/\partial I_v$ needed in this NR-algorithm, are calculated analytically. Our two-step procedure has the advantage of finding the threshold in almost any case without much effort from the user, who only has to define the initial position of the frequency window.

B. The DC Analysis

The nonlinear static problem is obtained by omitting the time derivatives and the noise sources in (5) and (11). Consider q_s modes. Given the static current excitations, the lasing wavelength $\tilde{\omega}_q$ and the optical power level of those q_s modes are found by transforming the boundary
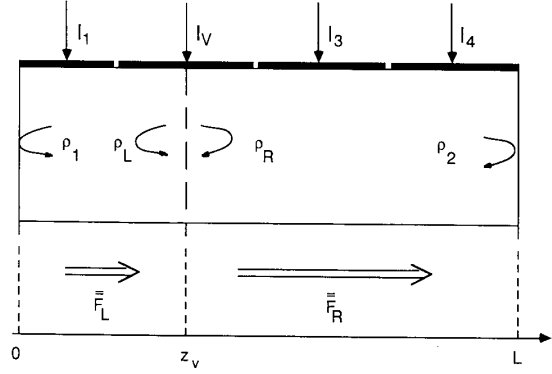

Fig. 3. Division of a laser in two parts for the calculation of the complex round-trip gain.

value problem (5)–(11) into an initial value problem that is solved with an iterative shooting method. As in our single-mode dc analysis of [7], this shooting method is also based on the propagator matrix formalism [2], [19].

To take into account the spatial variations of the carrier density along the cavity, each section j is divided into many small segments, in which the carrier density is considered to be uniform. However, in contrast to [7], we now need to include the spontaneous emission in the propagator matrices. For the ith segment, with length l_i, the propagator-matrix $\bar{\bar{F}}_{qi}$ of the qth mode then becomes

$$(\bar{\bar{F}}_{qi})_{11} = d_c \left[\cosh(D_q l_i) + j\frac{\Delta_q}{2D_q} \sinh(D_q l_i) \right]$$

$$(\bar{\bar{F}}_{qi})_{12} = 2jd_c \frac{\kappa^+}{2D_q} \sinh(D_q l_i)$$

$$(\bar{\bar{F}}_{qi})_{21} = 2jd_c \frac{\kappa^-}{2D_q} \sinh(D_q l_i)$$

$$(\bar{\bar{F}}_{qi})_{22} = d_c \left[\cosh(D_q l_i) - j\frac{\Delta_q}{2D_q} \sinh(D_q l_i) \right] \qquad (15)$$

with

$$d_c = \exp\left[\tfrac{1}{2}(g_{\text{sp}}^+ - g_{\text{sp}}^-) l_i\right]$$

$$\Delta_q = -2(\Delta\omega_q/v_{gq} + \Delta\beta_q) - j(g_{\text{sp}}^+ + g_{\text{sp}}^-)$$

$$D_q = [-\Delta_q^2/4 + \kappa^+\kappa^-]^{1/2}$$

$$g_{\text{sp}}^\pm = [J_{\text{sp}}/l_i] \int_i dz/|R_q^\pm|^2.$$

The $g_{\text{sp}}^\pm$ terms describe the spontaneous emission effects. The matrix $\bar{\bar{F}}_{qi}$ depends on the fields in segment i via the spontaneous emission, the spatial hole burning, and the nonlinear gain suppression. These dependencies imply a nonlinear wave propagation.

The propagation technique proceeds as follows. First, for each mode, an initial estimate is introduced for its lasing wavelength $\tilde{\omega}_q$ and for its backward field $R_q^-(z = 0)$,

which can be taken real without any restriction [see (4)]. Applying the left boundary condition gives the starting values for the q_s fields $R_q^+(z = 0)$. Both backward and forward waves of the q_s modes are then propagated through the laser taking the photon–carrier interaction into account self-consistently. Therefore the propagation through each segment $[z_{i-1}, z_i]$ requires a local iteration to find both the local carrier density and the $\overline{\overline{F}}_{qi}$ matrices. Once having arrived at the right facet ($z = L$) the second boundary condition requires $R_q^-(L) - \rho_2 R_q^+(L)$ to be zero. Since the propagation implies that $R_q^-(L)$ and $R_q^+(L)$ are complex functions of the real variables $\bar{\omega}_p$ and $R_q^-(0)$ with $p, q = 1, \cdots, q_s$, it is clear that we have to find the appropriate solution $[\bar{\omega}_1, R_1^-(0), \bar{\omega}_2, R_2^-(0), \cdots, \bar{\omega}_{q_s}, R_{q_s}^-(0)]$ of the set of q_s complex nonlinear coupled equations:

$$\left[R_q^-(L) - \rho_2 R_q^+(L) \right] \left[(\omega_p^-, R_p^-(0)); \right.$$
$$\left. p = 1, \cdots, q_s \right] = 0, \qquad (q = 1, \cdots, q_s). \quad (16)$$

A Newton–Raphson (NR) technique is applied to find this zero starting from the initial estimates. The derivatives needed in this NR algorithm are calculated by an additional nonlinear propagation of the $\partial R_q^\pm(z)/\partial \bar{\omega}_p$ and $\partial R_q^\pm(z)/\partial R_p^-(0)$ derivatives ($p, q = 1, \cdots, q_s$). The initial estimates pose no problem if the dc analysis is executed as described in Section IV.

With the carrier density and fields resulting from the dc analysis, CLADISS can also calculate the round-trip gain $\rho_L \rho_R$ above threshold for any frequency at any dc bias. The use of a single-mode dc analysis combined with the complex round-trip gain calculated above threshold over a wide frequency window allows to detect the onset of the side modes and is not as CPU time intensive as a self-consistent multimode dc analysis.

C. The AC Analysis

In this section we extend the single-mode ac analysis of [7] to a multimode ac analysis. Consider the q_s modes of the dc analysis. The usual approach towards the small-signal analysis is the sinus regime, written in the phasor notation. However, before complex phasors related to the modulation frequency $\Omega/2\pi$ can be introduced, the complex notation with respect to the optical reference frequency ω_q must be removed. Therefore, the complex fields $R_q^\pm(z, t)$ are replaced by their modulus $r_q^\pm(z, t)$ and phase $\phi_q^\pm(z, t)$ [see (4)]. For each mode the traveling-wave equations for r_q^+ and ϕ_q^+ then become (with $\Delta\beta_q = \Delta\beta_{rq} + j\Delta\beta_{iq}$)

$$\frac{\partial r_q^+}{\partial z} + \frac{1}{v_{gq}} \frac{\partial r_q^+}{\partial t} - \left(\Delta\beta_{iq} + \frac{J_{sp}}{(r_q^+)^2} \right) r_q^+$$
$$= -\left| \kappa^+ \right| \sin \left(\phi_\kappa^+ + \phi_q^- - \phi_q^+ \right) + F_{r,q}^+$$

$$\frac{\partial \phi_q^+}{\partial z} + \frac{1}{v_{gq}} \frac{\partial \phi_q^+}{\partial t} + \frac{1}{v_{gq}} \Delta\omega_q + \Delta\beta_{rq}$$
$$= \frac{r_q^-}{r_q^+} \left| \kappa^+ \right| \cos \left(\phi_\kappa^+ + \phi_q^- - \phi_q^+ \right) + F_{\phi,q}^+ \quad (17)$$

where ϕ_κ^+ is the phase of κ^+. The Langevin force functions $F_{r,q}^+$ and $F_{\phi,q}^+$ respectively, for the amplitude and the phase, again describe Gaussian processes. In the next section we will immediately give the statistical properties for these Langevin functions, instead of deriving them from the properties of F_q^+. For r_q^- and ϕ_q^- similar equations hold. Also, the boundary conditions at the laser ends and between two cascaded laser sections must be transformed into amplitude and phase expressions.

The sinus regime, with modulation frequency $\Omega/2\pi$, is now introduced by linearizing (11) and (17) and the appropriate boundary conditions around some bias point, using

$$r_q^\pm(z, t) = r_{q,0}^\pm(z) + \text{Re} \left(\Delta r_q^\pm(z, \Omega) \, e^{j\Omega t} \right)$$

$$\phi_q^\pm(z, t) = \phi_{q,0}^\pm(z) + \text{Re} \left(\Delta\phi_q^\pm(z, \Omega) \, e^{j\Omega t} \right)$$

$$N(z, t) = N_0(z) + \text{Re} \left(\Delta N(z, \Omega) \, e^{j\Omega t} \right)$$

$$J_j(t) = J_{j,0} + \text{Re} \left(\Delta J_j \, e^{j\Omega t} \right) \qquad (j = \text{section index})$$

$$\Delta\omega_q(t) = \Delta\omega_{q,0} + \text{Re} \left(\Delta\tilde{\omega}_q(\Omega) \, e^{j\Omega t} \right). \quad (18)$$

The terms with the subscript (0) belong to the static solution, while the other terms are small-signal complex phasors.

In the case of the ac analysis the noise sources are omitted and the only small-signal excitations are the modulation current densities ΔJ_j ($j = 1, \cdots, m_s$) superimposed on the bias current densities of the m_s sections. The small-signal equations thus obtained form a linear set of differential equations written in matrix form as

$$\frac{d\overline{X}}{dz}(z, \Omega) = \overline{\overline{A}}(z, \Omega) \, \overline{X}(z, \Omega) + \overline{B}(\Delta J_j, z, \Omega) \quad (19)$$

$$\overline{X} = \begin{pmatrix} X_1 \\ X_2 \\ \vdots \\ X_{q_s} \end{pmatrix} \quad \text{with}$$

$$X_q = \begin{pmatrix} \Delta\tilde{\omega}_q \\ \Delta r_q^+ \\ \Delta r_q^- \\ \Delta\phi_q^+ \\ \Delta\phi_q^- \end{pmatrix} \qquad (q = 1, \cdots, q_s). \quad (20)$$

The equations for $d\Delta\tilde{\omega}_q/dz$, included in (19), are the trivial identities $d\Delta\tilde{\omega}_q/dz = 0$. The matrices $\overline{\overline{A}}$ and $\overline{B}$ depend on the static solution of the bias point. Notice that the carrier density has been eliminated from (19). We will not give the linearized equations in any further detail because they are too extended, although their derivation is straightforward. By applying finite differences with the same longitudinal discretization scheme as in the dc analysis, (19) can be transformed into a set of linear algebraic

equations. Together with the linearized boundary conditions this linear set can be solved with standard techniques. $\Delta \tilde{\omega}_q(\Omega)$ then describes the FM response of the qth mode, while the IM response can be deduced from $\Delta r_q^-(0, \Omega)$ and $\Delta r_q^+(L, \Omega)$.

D. The Noise Analysis

Although several linewidth calculation techniques were developed for complex laser structures, to our knowledge none of them includes spatial hole burning [6] and multimode effects [18], [20] simultaneously. CLADISS however, does.

The noise analysis is based on the introduction in the laser equations (5) and (11) of Langevin forces that are both z- and t-dependent. Because the laser equations are derived in the slowly varying amplitude approximation, the Langevin forces must be regarded as the slowly-varying components of the carrier and photon fluctuations. However, quantities of practical interest, such as the linewidth ($\Delta\nu$) and the relative intensity noise (RIN), are also determined by slow variations (<10 GHz) of the frequency and the intensity. From the carrier scattering time (~ 0.1 ps) and length (~ 10 nm) it then follows that all Langevin forces are uncorrelated in time and longitudinal distance. The correlation functions of the Langevin forces, all assumed Gaussian with zero average, are derived in Appendix II and can be written as

$$\langle F_{r,q}^+(z, t)\, F_{r,q}^{+*}(z', t') \rangle$$
$$= 0.5 \Gamma g(\tilde{\omega}_q)\, \hbar\tilde{\omega}_q n_{sp}\delta(z - z')\, \delta(t - t')$$

$$\langle F_{\phi,q}^+(z, t)\, F_{\phi,q}^{+*}(z', t') \rangle$$
$$= (r_q^+)^{-2}\, \langle F_{r,q}^+(z, t)\, F_{r,q}^+(z', t') \rangle$$

$$F_N = F_S - \sum_q \frac{2r_q^+}{\hbar\tilde{\omega}_q wd} F_{r,q}^+ - \sum_q \frac{2r_q^-}{\hbar\tilde{\omega}_q wd} F_{r,q}^-$$

$$\langle F_S(z, t)\, F_S^*(z', t') \rangle$$
$$= \frac{2}{wd} \left\{ \frac{N}{\tau} + BN^2 + CN^3 \right\} \delta(z - z')\, \delta(t - t')$$

(21)

with n_{sp} being the inversion parameter. Similar relations hold for $F_{\phi,q}^-$ and $F_{r,q}^-$. Notice that, the Langevin forces in which F_N is decomposed, are all uncorrelated.

Usually, the Langevin forces only perturb the field quantities a little. This justifies a small-signal approximation. By subsequently Fourier transforming (11) and (17) and the Langevin forces, the sinus regime is introduced again. For each Fourier frequency $\Omega/2\pi$, the next set of linear differential equations results in

$$\frac{d\overline{X}}{dz}(z, \Omega) = \overline{\overline{A}}(z, \Omega)\, \overline{X}(z, \Omega) + \overline{C}(z, \Omega). \quad (22)$$

Here, $\overline{X}$ is given by (20), but now its elements describe the Fourier transformed stochastic perturbations ($\Delta r_q^\pm$,

$\Delta\phi_q^\pm$, $\Delta\tilde{\omega}_q$) of the field quantities. The elements of the source vector $\overline{C}$ are linear combinations of the Fourier transformed Langevin forces at the Fourier frequency $\Omega/2\pi$. Therefore, $\overline{C}$ is Gaussian with zero mean. Moreover, (21) shows that for two different Fourier frequencies, the corresponding spectral components of the Langevin forces are uncorrelated. Combining the above properties of $\overline{C}$ with a finite difference technique similar to the ac analysis, one can easily derive the correlation matrix $\langle \overline{X}(z, \Omega)\, \overline{X}^\dagger(z, \Omega') \rangle$ of $\overline{X}(z, \Omega)$. The superscript ($\dagger$) refers to the Hermitian matrix. To determine the intensity noise spectra at both laser facets, we need the correlation functions $\langle \Delta r_q^-(0, \Omega)\, \Delta r_q^{-*}(0, \Omega') \rangle$ and $\langle \Delta r_q^+(L, \Omega)\, \Delta r_q^{+*}(L, \Omega') \rangle$, which are elements of $\langle \overline{X}\overline{X}^\dagger \rangle$ at, respectively, $z = 0$ and $z = L$. The spectrum of the FM noise, the power spectrum, and the linewidth of the modes can be deduced from

$$\langle \Delta\tilde{\omega}_q(\Omega)\, \Delta\tilde{\omega}_q^*(\Omega') \rangle = 2D_{\tilde{\omega}_q}(\Omega)\, \delta(\Omega - \Omega') \quad (23)$$

which are elements of the matrix $\langle \overline{X}\overline{X}^\dagger \rangle$ for any z.

CLADISS offers two alternatives for the calculation of the linewidth and the power spectrum. The simplest approach is to approximate the FM noise spectrum by a white spectrum. This results in a Lorentzian power spectrum, with a linewidth given by

$$\Delta\nu_q = D_{\tilde{\omega}_q}(0)/(2\pi^2). \quad (24)$$

The second, more accurate approach, which incorporates the relaxation oscillation peaks, is based on the detailed numerical evaluation of the next approximate expression for the relative power spectrum of the qth mode [21]:

$$S_{\Delta P,q}(\omega) = F\left\{ \exp\left[j\tilde{\omega}_q\tau - 0.5 \right.\right.$$
$$\left.\left. \cdot \left\langle \left(\int_0^\tau \Delta\tilde{\omega}_q(t')\, dt' \right)^2 \right\rangle \right] \right\}. \quad (25)$$

Here F denotes the Fourier transform. The correlation function appearing in the exponent of (25) is related to $\langle \Delta\tilde{\omega}_q(\Omega)\, \Delta\tilde{\omega}_q(\Omega') \rangle$ via

$$\left\langle \left[\int_0^\tau \Delta\tilde{\omega}_q(t')\, dt' \right]^2 \right\rangle$$
$$= \frac{1}{2\pi^2} \int dt_1 \int dt_2 \int d\Omega\, 2D_{\tilde{\omega}_q}(\Omega)$$
$$\cdot \exp\left[j\Omega(t_1 - t_2) \right]. \quad (26)$$

The integrations in (25) and (26) are performed numerically.

VI. THE SOFTWARE IMPLEMENTATION AND ITS PERFORMANCE

CLADISS is a FORTRAN-77 program using single precision arithmetics. The I-O of CLADISS allows an efficient use in both interactive and batch runs. This is

TABLE III
TYPICAL CPU TIMES REQUIRED FOR THE ANALYSIS OF A SINGLE-SECTION 300 μm LONG DFB LASER[a]

Type of Analysis	Required CPU Time on a VAX Station 3200
Threshold Analysis for Two Modes	$\pm$2 min
dc Analysis for *I*: 30–100 mA P_f: 1–10 mW (Current Step: 0.5 mA)	Single-Mode Calculation: $\pm$ 20 min Two-Mode Calculation: $\pm$60 min
Solution of the system of small-signal equations for a set of 30 modulation frequencies (ac analysis, noise analysis)	Single-Mode Calculation: $\pm$7 s Two-Mode Calculation: $\pm$24 s

[a]Longitudinal discretization step: $l_i = 12\ \mu$m.

TABLE IV
PARAMETER CHARACTERISTICS OF LASERS *A*, *B*, AND *C*, RESPECTIVELY

Case	R_b	ϕ_b	R_f	ϕ_f	L [μm]	κL
A	0.32	π	0.05	$3\pi/2$	300	2
B	0.32	$\pi/4$	0	—	300	2
C	0.32	π	0.05	$3\pi/2$	600	3

TABLE V
THRESHOLD CHARACTERISTICS

Case	I_{th} [mA]	λ_{th} [μm]	$\Delta\alpha L$
A	22.05	1.5618	0.28
B	25.05	1.5616	0.32
C	39.56	1.5616	0.25

mainly achieved through the development of a CLADISS Command Language (CCL). The CCL commands issued to CLADISS specify the type of analysis to be performed, the type of output (file, screen, tables, plots) that is desired, and the operating range that must be investigated. Table III shows some typical CPU times CLADISS needs to perform certain calculations. As an example a DFB laser was taken and the calculations were done on a DEC VAX station 3200 (8 Mips).

VII. EXAMPLES ON DFB LASERS

The model has already been applied to a large number of laser diodes, including tunable three-section DBR lasers, $\lambda/4$-phase-shifted DFB lasers, and external cavity DFB lasers. Some results have been presented in [7]–[9], [12], [13]. In this section we illustrate the capabilities of CLADISS by means of three examples of DFB lasers, labeled *A*, *B*, and *C*. Their common parameter values are listed in Table I, whereas parameter values specific to each of them are given in Table IV.

Table V contains the values of the threshold current I_{th} and the threshold gain difference $\Delta g L$ for *A*, *B*, and *C*. The large values of $\Delta g L$ suggest single-mode behavior for each laser [22]. This expectation is sustained by Fig. 4, which shows the complex round-trip gain at threshold for each of the devices. Both the main mode and the strongest side mode are indicated by an arrow.

A. The DC Behavior of a DFB Laser

The threshold analysis does obviously not give any information about spatial hole burning effects and therefore large values of $\Delta g L$ do not always guarantee a stable single-mode behavior up to high-power levels. Consequently, a yield analysis based only on the threshold gain difference at threshold may be erroneous [1].

Therefore, some authors [1], [5] also determine the threshold gain difference above threshold, so that the spatial hole burning caused by the main mode can be taken into account. This implies a single-mode dc analysis. CLADISS goes a step further by explicitly calculating the power in the sidemodes. In Fig. 5 this is illustrated for

the laser *C*, where the main and the first side mode are depicted. A clear deterioration of the side-mode suppression ratio is observed. Around 70 mA the strongest side mode reaches its threshold. This is confirmed by Fig. 6, which shows the complex round-trip gain, including spatial hole burning effects, for 70 mA. Comparison of Fig. 4(c) and Fig. 6 confirms the detrimental effect of the spatial hole burning in this particular case.

The influence of spatial hole burning can be seen from the longitudinal variation of the real part of the Bragg deviation $\Delta\beta_q$, which is depicted in Fig. 7 for the main mode ($q = 1$) and the strongest side mode ($q = 2$) of laser *C* at different bias levels. As the current increases, the Bragg deviation $|\text{Re}\,(\Delta\beta_2)|$ of the side mode decreases near the laser facets, while the Bragg deviation $|\text{Re}\,(\Delta\beta_1)|$ of the main mode increases. Since the loss associated with the Bragg reflections decreases for decreasing Bragg deviations, it follows that the average loss of the side mode decreases, while the loss of the main mode increases. Due to gain clamping this also implies a gain increase. The increased gain and the decreased loss of the side mode can then result in the onset of the side mode. The variation of the Bragg deviation is obviously caused by the variation of the carrier density and the carrier-induced refractive index, which in turn is due to the longitudinal variation of the optical power (spatial hole burning).

The influence of longitudinal spatial hole burning on the single-mode stability increases for increasing values of κ and L. Indeed, large values of κ and L give rise to strong spatial hole burning, with the power being more concentrated near the center of the laser. At the same time however, the spatial hole burning has also more influence since the Bragg reflections have a larger impact on the laser behavior. Both lasers *A* and *B*, which are only half as long as laser *C*, exhibit a stable single-mode behavior up to high-power levels, as is illustrated in Fig. 8 (laser *A*) and in Fig. 9 (laser *B*). The side-mode rejection of *A* and *B* remains more than 35 dB up to at least 20 mW output power.
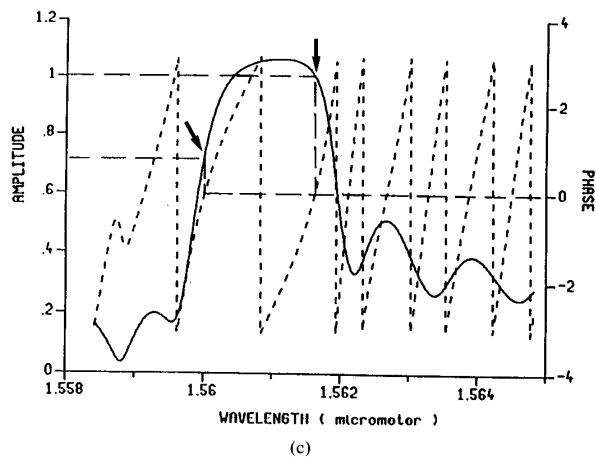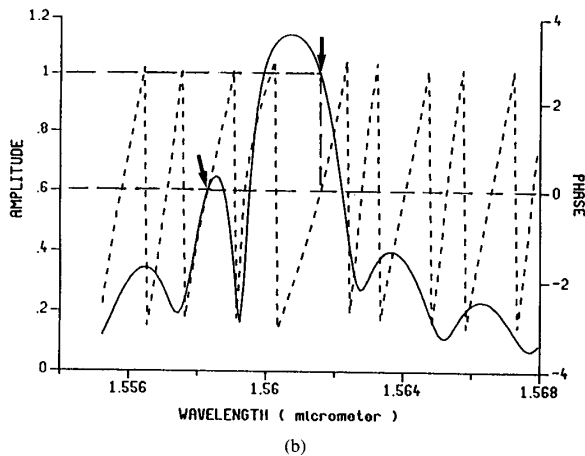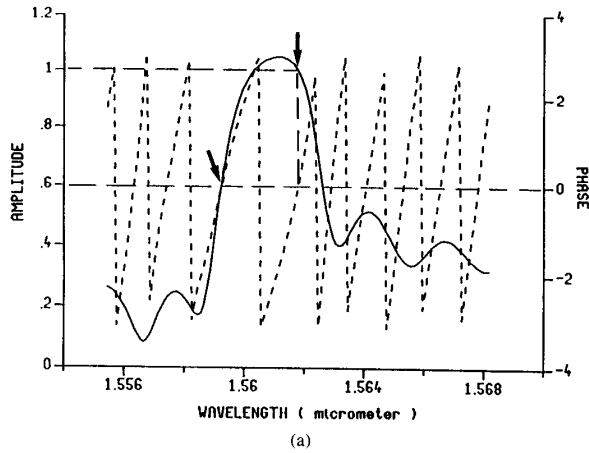
(a)

(b)

(c)

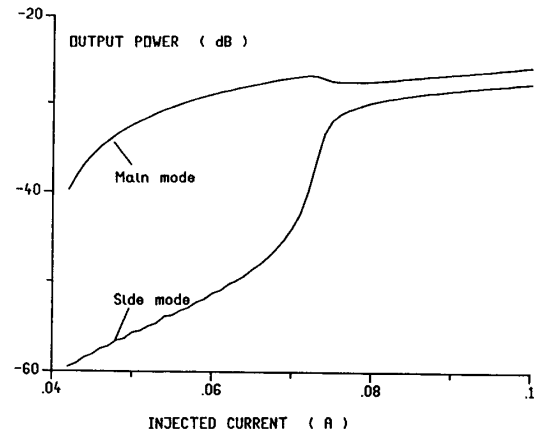Fig. 4. (a) Amplitude (solid line) and phase (broken line) of the complex round-trip gain at the laser threshold current as a function of wavelength for laser A. (b) Amplitude (solid line) and phase (broken line) of the complex round-trip gain at the laser threshold current as a function of wavelength for laser B. (c) Amplitude (solid line) and phase (broken line) of the complex round-trip gain at the laser threshold current as a function of wavelength for laser C.

Fig. 5. Output power of main and side mode at the front facet versus injected current for laser C.
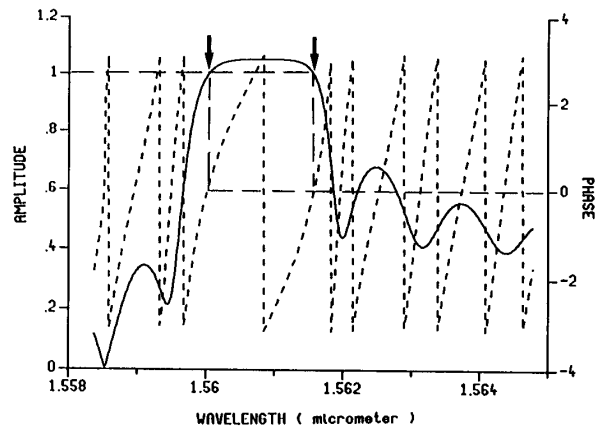
Fig. 6. Amplitude (solid line) and phase (broken line) of the complex round-trip gain at the threshold current of the side mode ($I = 70$ mA) as a function of wavelength for laser C.

B. The AC Behavior of a DFB Laser

So far, the ac model has mainly been used to study the carrier-induced FM response in DFB lasers. Experimentally, a number of anomalies, either as a function of modulation frequency or as a function of bias level, are found in the FM response of DFB lasers. Simulations with CLADISS have shown that these anomalies can be well explained by spatial hole burning [7].

The influence of spatial hole burning on the FM is illustrated for the single-mode lasers A and B. No influence of the side modes on the FM response can be detected numerically for these lasers. The FM response including the spatial hole burning contribution, is depicted in Fig. 10 for laser A and in Fig. 11 for laser B. Nonlinear gain suppression has been neglected in the calculations. It is seen that for low modulation frequencies the spatial hole burning contribution can either be in phase (device A) or out of phase (device B) with the modulation current.
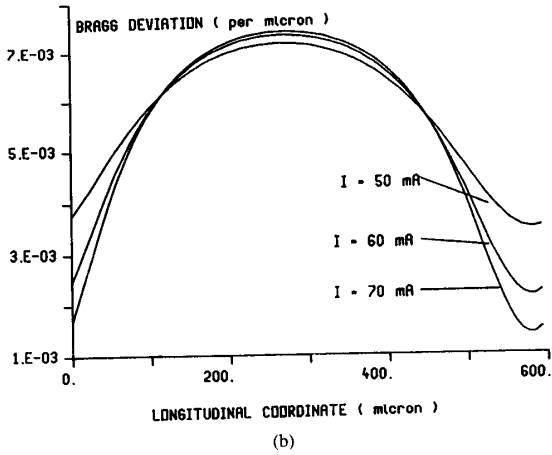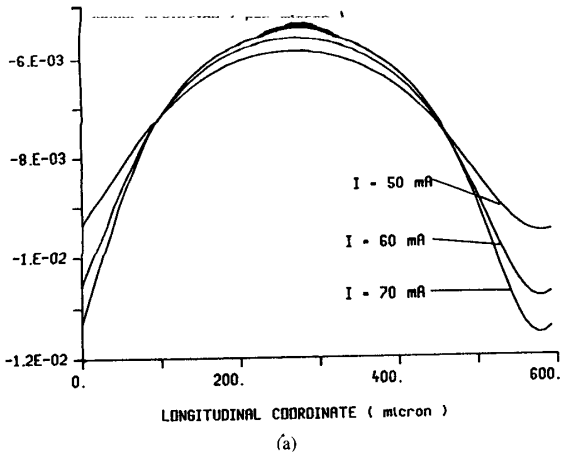
(a)

(b)

Fig. 7. Longitudinal variation of the real part of the Bragg deviation $\Delta\beta_q$ in laser C; (a) main mode ($q = 1$), (b) side mode ($q = 2$).
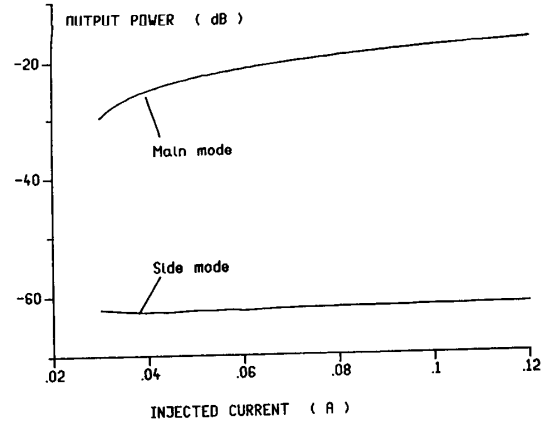

Fig. 9. Output power of main and side mode at the front facet versus injected current for laser B.
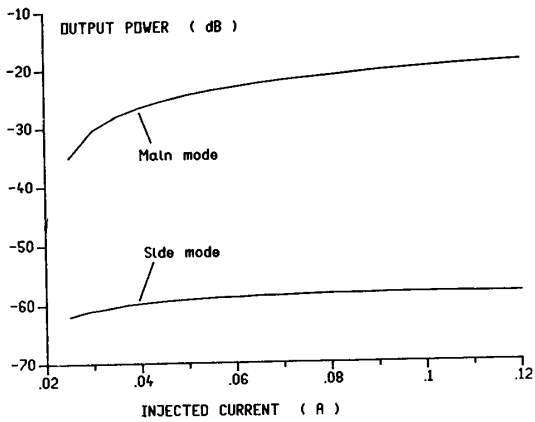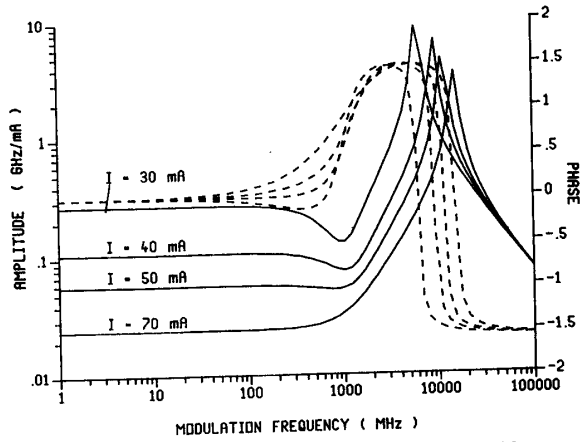

Fig. 10. Amplitude (solid line) and phase (broken line) of the FM response for laser A including the spatial hole burning contribution.

Fig. 8. Output power of main and side mode at the front facet versus injected current for laser A.
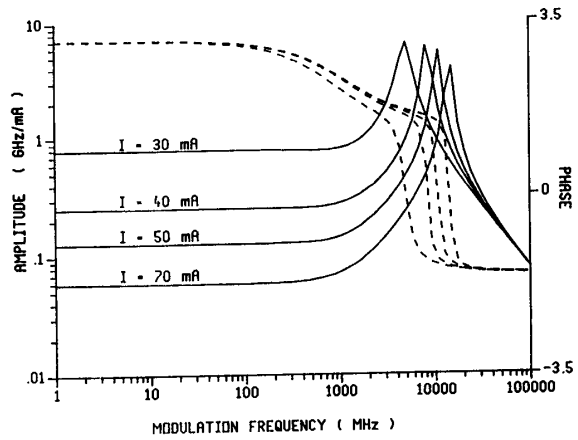

Fig. 11. Amplitude (solid line) and phase (broken line) of the FM response for laser B including the spatial hole burning contribution.

Some influence of side modes on the FM response can be seen for laser C. Fig. 12 shows the amplitude and the phase of the FM response at a bias current of 70 mA, calculated with and without taking into account the influence of the side mode. The relative side-mode intensity is -17 dB at this bias level and causes only a small increase of the FM response. In this example, nonlinear gain suppression ($\epsilon_{sp} = 15$ W^{-1}) is also taken into account, which explains the strong damping of the relaxation oscillation.

C. The Linewidth of a DFB Laser

A phenomenon that is often observed, but that is not quite fully understood is the presence of a linewidth floor. Possible mechanisms to explain this effect, such as the influence of side modes, nonlinear gain suppression, and spatial hole burning have been investigated with CLAD-ISS.

The linewidth floor can be caused by the onset, as shown in [23], which influences the main mode through *spectral* hole burning. The side-mode effects in the linewidth, however, occur only for relative side-mode intensities above -30 to -20 dB. We show that the influence of the onset of a side mode on the linewidth of the main mode can also be attributed to other nonlinearities. We found that the onset of side modes in a DFB laser can also affect the main-mode linewidth through *spatial* hole burning. This is illustrated in Fig. 13, where the linewidth of laser C is depicted. Spectral hole burning is neglected in this calculation and the linewidth rebroadening at the onset of the side mode is due to longitudinal spatial hole burning. Once the side mode has reached its lasing threshold, the linewidth is seen to decrease again. In this case the lasing of the side mode results in additional carrier clamping and the fluctuations of the carrier density and hence the linewidth will be mainly proportional to the inverse of the side-mode power.

Experimentally however, a weak rebroadening or a saturation of the linewidth also occurs for side-mode suppression ratios of more than 30 dB up to high-power levels, as in lasers A and B. An explanation for this, first suggested by Agrawal in [24] and by the authors in [8], is the power dependence of the linewidth enhancement factor α_{lw} due to gain nonlinearities, e.g., spectral hole burning. If the nonlinearity causes a gain suppression which is quasi-symmetric around the lasing wavelength, it will hardly influence the refractive index. Consequently, it follows from (6) that for a single-mode situation ($q = 1$), the linewidth enhancement factor α_{lw} can be written as

$$\alpha_{lw}(\tilde{\omega}_q) = \frac{\alpha_{lw,0}(\tilde{\omega}_q)}{1 - \epsilon_{sp}(\tilde{\omega}_q, \tilde{\omega}_q)P_q}. \qquad (27)$$

This effect is illustrated in Fig. 14 for laser A. The linewidth minimum occurs for an average intracavity power of approximately $1/(3\epsilon_{sp}(\tilde{\omega}_q, \tilde{\omega}_q))$. The value used for the gain suppression coefficient $\epsilon_{sp}(\tilde{\omega}_q, \tilde{\omega}_q)$ is 15 W^{-1} and has the same order of magnitude as the experimental value
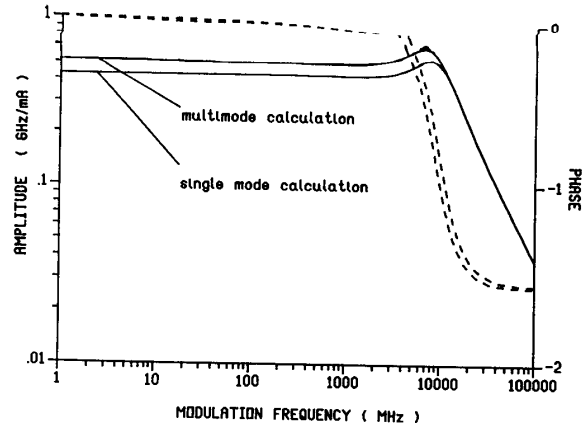

Fig. 12. Amplitude (solid line) and phase (broken line) of the FM response for laser C at 70 mA bias: influence of the side mode when both spatial hole burning and nonlinear gain suppression ($\epsilon_{sp} = 15$ W^{-1}) are taken into account.
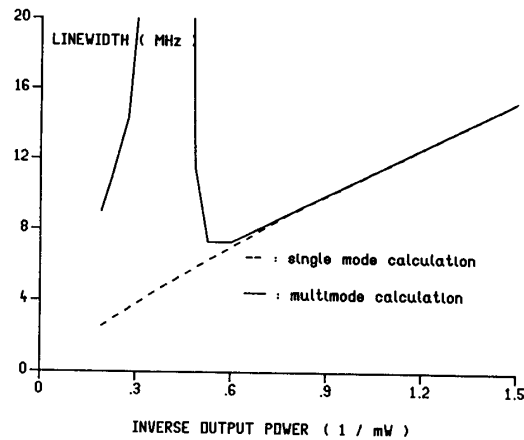

Fig. 13. Influence of the side mode on the linewidth of the main mode for laser C when only spatial hole burning is taken into account.

obtained in [25]. It must be noted here that apart from spectral hole burning, other gain nonlinearities such as carrier-dependent dispersion or the formation of gratings by cavity standing waves can also cause a gain suppression without affecting the refractive index. The exact power dependence of the α_{lw}-factor obviously strongly depends on the functional form used for the gain suppression.

Fig. 15 shows the calculated linewidth for laser B. The linewidth rebroadening is less pronounced and occurs at higher power levels in this case. The difference between lasers A and B results from spatial hole burning. Spatial hole burning causes an increase of the threshold gain and of the spontaneous emission rate with increasing power for laser A, but a decreasing threshold gain and spontaneous emission rate for laser B. This partly compensates the effect of the power dependence of the α-factor for laser B. In both lasers A and B, no influence of the side modes
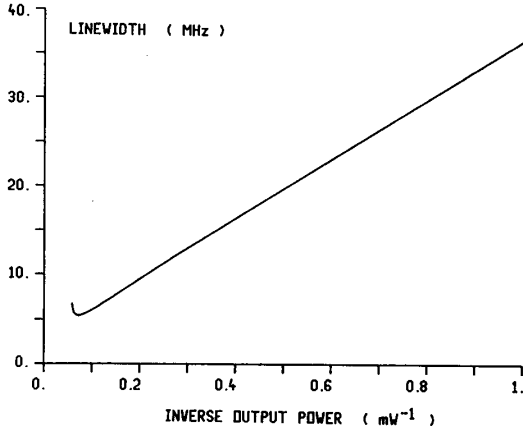
Fig. 14. Linewidth rebroadening of a single-mode laser (laser A) due to spatial hole burning and nonlinear gain suppression.
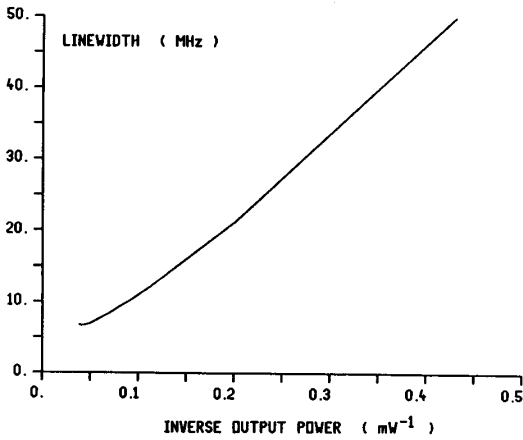

Fig. 15. Linewidth saturation of a single-mode laser (laser B) due to spatial hole burning and nonlinear gain suppression.

on the main mode linewidth could be detected numerically.

VIII. CONCLUSION

We have shown how the multimode behavior of a general multisection diode laser with or without distributed feedback can be described by a set of (z, t)-dependent differential equations, that include longitudinal spatial hole burning, nonlinear gain suppression, spontaneous emission, and noise. Next, we have indicated how these equations are solved in threshold, dc, ac, and noise analyses. The essential differences between those four types of analysis are summarized in Table II while an overview of the laser characteristics that can be calculated by them is given in Fig. 2. The four types of analysis have been implemented in the CLADISS simulator tool, which is, to our knowledge, one of the most advanced diode laser simulators at present. In particular, the multimode character and the inclusion of longitudinal spatial hole burning are unique features.

To demonstrate the capabilities of CLADISS some examples illustrating essential properties of DFB lasers are discussed in Section VII. The first example shows how the single-mode behavior of a DFB laser can deteriorate due to spatial hole burning, even when a very large threshold gain difference occurs at the laser threshold. Therefore the usual criterion [22] which claims that DFB lasers with a threshold gain difference larger than some critical value are single-mode devices should be regarded with sufficient care. The second example demonstrates that the spatial hole burning contribution to the FM response of a DFB laser can either show a red or a blue frequency shift. Moreover, we found that at a 30 dB down level the side modes have no effect at all on the FM response. Finally, in the third example we point out that for DFB lasers with a good mode rejection ratio, i.e., greater than about 30 dB at a power level of 5 mW, the linewidth floor is due to the power dependence of the linewidth enhancement factor, caused by gain nonlinearities. Notice also that a large gain suppression gives a large FM efficiency at low and intermediate (<1 GHz) modulation frequencies. But on the other hand, a high-gain suppression level causes the linewidth floor to occur at lower power levels. Both effects are due to the incomplete carrier clamping induced by the gain suppression. We also showed that the onset of side modes can induce a linewidth floor through the spatial hole burning.

APPENDIX I
SPONTANEOUS EMISSION

The form of the spontaneous emission terms in the wave equations (5) can be justified as follows. Consider the next wave equations, in which any noise sources are omitted to simplify the calculations:

$$\pm \frac{\partial R_q^{\pm}}{\partial z} + \frac{1}{v_{gq}} \frac{\partial R_q^{\pm}}{\partial t} + \left(j \frac{\Delta \omega_q}{v_{gq}} + j \Delta \beta_q \right) R_q^{\pm}$$

$$= j\kappa^{\pm} R_q^{\mp} + T_q^{\pm}. \tag{28}$$

$T_q^{\pm}$ represents the fraction of the locally and spontaneously emitted photons that couple with the qth mode $R_q^{\pm}$. We now replace the complex amplitudes $R_q^{\pm}$ in the wave equation (28) by $r_q^{\pm} \exp (j \phi_q^{\pm})$ and retain only the real part of the resulting identities. After multiplication with $2 r_q^{\pm}$ we obtain the intensity equations

$$\pm \frac{\partial I_q^{\pm}}{\partial z} + \frac{1}{v_{gq}} \frac{\partial I_q^{\pm}}{\partial t}$$

$$= 2 \operatorname{Im} (\Delta \beta_q) I_q^{\pm} + 2 \operatorname{Re} \left(T_q^{\pm} (R_q^{\pm})^* \right)$$

$$+ 2 \operatorname{Re} \left(j\kappa^{\pm} R_q^{\mp} (R_q^{\pm})^* \right). \tag{29}$$

The asterisk indicates complex conjugation and $I_q^{\pm}$ equals $|R_q^{\pm}|^2$. The total spontaneous emission integrated over the entire spectrum is equal to the radiative (i.e., bimolecular) spontaneous recombination. Expressed in the number of photons generated per unit time and per unit volume, it can be written as BN^2. Only a fraction of the sponta-

neous emission couples into the qth mode. Therefore, we can state that

$$2 \, \mathrm{Re} \left(T_q^{\pm} (R_q^{\pm})^* \right) = \tfrac{1}{2} \beta_{sp} wd \, (\hbar \omega_q) B N^2. \tag{30}$$

The above relation expresses $2 \, \mathrm{Re} \, (T_q^{\pm}(R_q^{\pm})^*)$ as a source term for the intensity, in analogy with the spontaneous emission source in the local photon continuity equations derived by Lamb for Fabry–Perot laser amplifiers [26]. The factor $1/2$ indicates that the emission that is coupled into a mode is divided equally over the forward and backward waves; β_{sp} is the spontaneous emission factor, including Petermann's K-factor [16]. Because it is the in-phase spontaneous emission that couples into the mode, we assume $T_q^{\pm}$ to be in-phase with $R_q^{\pm}$. We then get

$$T_q^{\pm} = \frac{\beta_{sp}}{4(R_q^{\pm})^*} wd \, (\hbar \omega_q) B N^2 = \frac{J_{sp}}{|R_q^{\pm}|^2} R_q^{\pm}. \tag{31}$$

The second identity defines J_{sp}.

APPENDIX II
CORRELATION OF THE LANGEVIN NOISE SOURCES

The second-order moments of the Langevin forces can be derived by rigorously transforming the generalized Helmholtz equation for the electric field into coupled wave equations [17].

Here we present a more intuitive derivation. It is based on the transformation of (17) into rate equations. Therefore, we introduce the total derivatives with respect to time for the forward and backward propagating waves:

$$\frac{d}{dt_f} = \frac{\partial}{\partial t} + \frac{1}{v_{gq}} \frac{\partial}{\partial z} \quad \text{and}$$

$$\frac{d}{dt_b} = \frac{\partial}{\partial t} - \frac{1}{v_{gq}} \frac{\partial}{\partial z}. \tag{32}$$

Using those derivatives (17) can be written as

$$\frac{1}{v_{gq}} \frac{dr_q^+}{dt_f} - \left(\Delta \beta_{iq} + \frac{J_{sp}}{(r_q^+)^2} \right) r_q^+$$

$$= - \left| \kappa^+ \right| r_q^+ \sin \left(\phi_\kappa^+ + \phi_q^- - \phi_q^+ \right) + F_{r,q}^+$$

$$\frac{1}{v_{gq}} \frac{d\phi_q^+}{dt_f} + \frac{1}{v_{gq}} \Delta \omega_q + \Delta \beta_{rq}$$

$$= \frac{r_q^-}{r_q^+} \left| \kappa^+ \right| \cos \left(\phi_\kappa^+ + \phi_q^- - \phi_q^+ \right) + F_{\phi,q}^+ \tag{33}$$

Multiplication of the first equation with $(2r_q^+/\hbar \tilde{\omega}_q)$ and the integration over a segment l_i results in a rate equation for the number of forward propagating photons i_q^+ in the segment l_i:

$$\frac{1}{v_{gq}} \frac{di_q^+}{dt_f} - 2\Delta \beta_{iq} i_q^+ - \frac{2J_{sp}}{\hbar \tilde{\omega}_q}$$

$$= \frac{2}{\hbar \tilde{\omega}_q} \, \mathrm{Re} \left(j \kappa^+ R_q^- R_q^{+*} l_i \right) + F_{i,q}^+ \tag{34}$$

with

$$F_{i,q}^+ = (\hbar \tilde{\omega}_q)^{-1} \int_{l_i} dz \, 2r_q^+ F_{r,q}^+(z, t). \tag{35}$$

The correlation function of the Langevin force appearing in a photon rate equation has been derived before [18]:

$$\langle F_{i,q}^+(t) \, F_{i,q}^{+*}(t') \rangle = 2 R i_q^+ \delta(t - t'). \tag{36}$$

The correlation function of $F_{r,q}^+$ can then be calculated with the help of (35), by assuming the field amplitudes to be constant in the small segments and by taking into account that

$$R = \Gamma g(\tilde{\omega}_q) v_g n_{sp}. \tag{37}$$

The correlation functions of $F_{r,q}^-$ and $F_{\phi,q}^{\pm}$ can be derived in a similar way.

REFERENCES

[1] H. Soda, Y. Kotaki, H., Sudo, H. Ishikawa, S. Yamakoshi, and H. Imai, "Stability in single longitudinal mode operation in Ga-InAsP/InP phase-adjusted DFB lasers," *IEEE J. Quantum Electron.*, vol. QE-23, pp. 804–814, June 1987.

[2] G. Björk and O. Nilsson, "A new exact and efficient numerical matrix theory of complicated laser structures: Properties of asymmetric phase-shifted DFB lasers," *J. Lightwave Technol.*, vol. LT-5, pp. 140–146, Jan. 1987.

[3] G. Agrawal and A. Bobeck, "Modeling of distributed feedback semiconductor lasers with axially-varying parameters," *IEEE J. Quantum Electron.*, vol. 24, pp. 2407–2414, Dec. 1988.

[4] X. Pan, H. Olesen, and B. Tromborg, "A theoretical model of multielectrode DBR lasers," *IEEE J. Quantum Electron.*, vol. 24, pp. 2423–2432, Dec. 1988.

[5] W. Rabinovich and B. Feldman, "Spatial hole burning effects in distributed feedback lasers," *IEEE J. Quantum Electron.*, vol. 25, pp. 20–30, Jan. 1989.

[6] J. Whiteaway, G. Thompson, A. Collar, and C. Armistead, "The design and assessment of λ/4 phase-shifted DFB laser structures," *IEEE J. Quantum Electron.*, vol. 25, pp. 1261–1279, June 1989.

[7] P. Vankwikelberge, F. Buytaert, A. Franchois, R. Baets, P. Kuindersma, and C. Frederiksz, "Analysis of the carrier-induced FM response of DFB lasers: Theoretical and experimental case studies," *IEEE J. Quantum Electron.*, vol. 25, pp. 2239–2254, Nov. 1989.

[8] G. Morthier, P. Vankwikelberge, F. Buytaert, R. Baets, and P. Lagasse, "Linewidth of single mode DFB lasers in the presence of spatial and spectral hole burning," presented at *Proc. Euro. Conf. Opt. Commun.—ECOC '89*, Gothenburg, Sweden, Sept. 1989.

[9] G. Morthier, P. Vankwikelberge, F. Buyaert, and R. Baets, "Influence of gain non-linearities on the linewidth enhancement factor in semiconductor lasers," *IEE Proc.*, Pt. J, vol. 137, pp. 30–32, Feb. 1990.

[10] M. Schubert and B. Wilhelmi, *Nonlinear Optics and Quantum Electronics*. New York: Wiley, 1986, ch. 1, sec. 1.4.2.

[11] D. Marcuse, *Theory of Dielectric Optical Waveguides*. New York: Academic, 1974, ch. 3.

[12] G. Morthier, P. Vankwikelberge, K. David, and R. Baets, "Improved performance of AR-coated DFB-lasers by the introduction of gain-coupling," *IEEE Photon. Technol. Lett.*, vol. 2, pp. 170–172, Mar. 1990.

[13] K. David, G. Morthier, P. Vankwikelberge, and R. Baets, "Yield analysis of DFB lasers with various facet reflectivities and degrees of

gain coupling," *Electron. Lett.*, vol. 26, no. 4, pp. 238-239, Feb. 15, 1990.

[14] C. Henry, R. Logan, F. Merritt, and J. Luongo, "The effect of intervalence band absorption on the thermal behavior of InGaAsP lasers," *IEEE J. Quantum Electron.*, vol. QE-19, pp. 947-952, June 1983.

[15] M. Asada and Y. Suematsu, "Density-matrix theory of semiconductor lasers with relaxation broadening model–Gain and gain-suppression in semiconductor lasers," *IEEE J. Quantum Electron.*, vol. QE-21, pp. 434-442, May 1985.

[16] K. Petermann, "Calculated spontaneous emission factor for double-heterostructure injection lasers with gain-induced waveguiding," *IEEE J. Quantum Electron.*, vol. QE-15, pp. 566-570, July 1979.

[17] C. Henry, "Theory of the phase noise and power spectrum of a single-mode injection laser," *IEEE J. Quantum Electron.*, vol. QE-19, pp. 1391-1397, Sept. 1983.

[18] ——, "Theory of spontaneous emission noise in open resonators and its application to lasers and optical amplifiers," *J. Lightwave Technol.*, vol. LT-4, pp. 288-297, Mar. 1986.

[19] M. Yamada and K. Sakuda, "Analysis of almost-periodic distributed feedback slab waveguides via a fundamental matrix approach," *Appl. Opt.*, vol. 26, pp. 3474-3478, Aug. 15, 1987.

[20] G. Björk and O. Nilsson, "A tool to calculate the linewidth of complicated semiconductor lasers," *IEEE J. Quantum Electron.*, vol. 23, pp. 1303-1313, Aug. 1987.

[21] K. Vahala and A. Yariv, "Semiclassical theory of noise in semiconductor lasers—Part II," *IEEE J. Quantum Electron.*, vol. 19, pp. 1102-1109, June 1985.

[22] P. Mols, P. Kuindersma, W. van Es-Spiekman, and I. Baele, "Yield and device characteristics of DFB lasers: Statistics and novel coating design in theory and experiment," *IEEE J. Quantum Electron.*, vol. 25, pp. 1303-1313, June 1989.

[23] U. Kruger and K. Petermann, "The semiconductor laser linewidth due to the presence of side modes," *IEEE J. Quantum Electron.*, vol. 24, pp. 2355-2358, Dec. 1988.

[24] G. Agrawal, "Intensity dependence of the linewidth enhancement factor and its implications for semiconductor lasers," *IEEE Photon. Technol. Lett.*, vol. 1, pp. 212-214, Aug. 1989.

[25] R. S. Tucker, "High-speed modulation of semiconductor lasers," *J. Lightwave Technol.*, vol. LT-3, pp. 1180-1192, Dec. 1985.

[26] A. Icsevgi and W. Lamb, "Propagation of light pulses in a laser amplifier," *Phys. Rev.*, vol. 185, pp. 517-545, Sept. 1969.

Patrick Vankwikelberge was born in Ghent, Belgium, on May 20, 1962. He received the electrical engineering degree in 1985 and the Ph.D. degree, also in electrical engineering, in 1990, both from the University of Ghent.

Currently, he is engaged in research on the dynamic behavior of semiconductor lasers with the Laboratory of Electromagnetism and Acoustics, University of Ghent.

Geert Morthier was born in Ghent, Belgium, on March 20, 1964. He received the electrical engineering degree from the University of Ghent in 1987.

He is presently working toward the Ph.D. degree in electrical engineering at the Laboratory of Electromagnetism and Acoustics, University of Ghent. His main research interests are the spectral and dynamic properties of semiconductor lasers.

Roel Baets (M'88) received the degree in electrical engineering from the University of Ghent, Belgium, in 1980, the M.Sc. degree in electrical engineering from Stanford University, Stanford, CA, in 1981, and the Ph.D. degree from the University of Ghent in 1984.

Since 1984 he has been with the Interuniversity Micro-Electronics Centre (IMEC) and works in the Laboratory of Electromagnetism and Acoustics, University of Ghent, where he is head of research on optoelectronic devices. He lectures part-time courses on optoelectronics at the University of Ghent. His research interests include both the theory and technology of optoelectronic devices, especially laser diodes and optical waveguides and switches.

Dr. Baets is a member of the Optical Society of America.